Research in Astron. Astrophys. **2013** Vol. **13** No. **5**, 604–614
http://www.raa-journal.org *http://www.iop.org/journals/raa*

Research in Astronomy and Astrophysics

A new source extraction algorithm for optical space debris observation *

Rong-Yu Sun[1,2,3] and Chang-Yin Zhao[1,2]

[1] Purple Mountain Observatory, Chinese Academy of Sciences, Nanjing 210008, China; *rysun@pmo.ac.cn*
[2] Key Laboratory of Space Object and Debris Observation, Chinese Academy of Sciences, Nanjing 210008, China
[3] Graduate University of Chinese Academy of Sciences, Beijing 100049, China

Received 2012 September 5; accepted 2012 November 12

Abstract Specific challenges arise in the task of real-time automatic data reduction of optical space debris observations. Here we present an automatic technique that optimally detects and measures the sources from images of optical space debris observations. We show that highly reliable and accurate results can be obtained on most images produced by our specific sensors, and due to optimizations, the whole pipeline works fast and efficiently. Tests demonstrate that the technique performs better than SExtractor from the point of view of fast and accurate detection, therefore it is well suited for data reduction of optical space debris observations.

Key words: techniques: image processing — space vehicles — astrometry

1 INTRODUCTION

Space debris is defined as non-functional artificial objects of all sizes in near-earth space, and has been recognized as an increasing threat for current and future space operations (Schildknecht 2007). Nowadays there are more than 14 000 objects cataloged by the US Strategic Command (USSTRATCOM), in geocentric orbits with altitudes ranging from 300 km to 40 000 km. To avoid the risk caused by space debris in space missions, information about such objects must be continuously collected and maintained. Due to the fact that near-earth objects can be illuminated by the Sun during nighttime, optical observation is a feasible and realistic technique for space debris detection. To date, several countries and organizations have carried out optical space debris surveys and published their results (Schildknecht et al. 2001, 2004, 2008; Rykhlova et al. 2001; Seitzer et al. 2004; Molotov et al. 2008; Porfilio et al. 2004; Alby et al. 2004; Musci et al. 2004, 2005; Hebert et al. 2001; Sun & Zhao 2012).

Similar to the planets, minor planets and comets in the solar system, near-earth space debris moves with respect to the background stars, and hence there is a relative movement between space debris and background stars during exposure. To optimize the signal-to-noise ratio (SNR) of objects, an alternative observation strategy is adopted in optical observation, in particular, for objects in low Earth orbit, which move fast with respect to the stars. CCD images are obtained as the process for

* Supported by the National Natural Science Foundation of China.

tracking objects is applied, and for Geosynchronous Orbit (GEO) objects, which move slowly with respect to the stars, the drive is turned off during exposure. Such a strategy shows the images of objects of interest as points, while the background stars appear as streaks, and the trail length of the stars depends on the exposure time and the relative velocity of the telescope.

After the CCD images are taken, the detection of the debris objects in the images crucially depends on the source extraction algorithm used. To detect the debris efficiently and in time, while maintaining high precision in terms of position, an advanced algorithm must satisfy several requirements: first, the time cost of processing, including the discrimination and extraction of both stars and debris, must be smaller than the exposure interval, so the data can be handled in real-time; then, due to the generally large field of view (FOV) of telescopes, the algorithm must be able to withstand large variations in noise, e.g. bright night-sky background or the presence of clouds; and finally, for high precision astrometric calibration, the centers of the objects obtained must be accurate enough. In addition, specific problems arise if the shutter of the camera is removed because of the high frame rate in observation, which makes the smear noise ineluctable (Sun et al. 2012a,b), and due to the relative movement between objects and stars, the blending of images is also sometimes inevitable (Sun et al. 2012c); both cases make the data reduction more difficult and reduce the precision in determining the position of objects, and hence they must be handled properly in the algorithm.

To resolve the above problems, an algorithm based on mathematical morphology is presented. By the use of a top-hat operator and an innovative structure element (if needed), the objects can be detected with a high degree of precision for computing the centroid. The method is well-suited for processing the CCD images of optical space debris.

2 IMAGE PROCESSING ALGORITHM

2.1 Mathematical Morphology Methods

Mathematical morphology is a field of study focusing on the analysis and processing of geometrical structures, which incorporates ideas from set theory, lattice theory, topology, and random functions. The transformations of such methods use a structure element, which includes a special set of pixels in the image and can be defined as any geometric shape with a fixed center. It has been implemented in the identification of GEO objects and has been shown to work well (Laas-Bourez et al. 2012). During transformation, the whole image is scanned by the structure element and each pixel is given a value according to the pixel values included in the structure element, while the center of the structure element coincides with the investigated pixel. The transformation is composed of two basic operators: erosion and dilation. These two transformations of a grey level image $f(x)$ by structure element (SE) are defined as:

$$\begin{cases} D^{\mathrm{SE}}(f(x)) = \max\{f(x+y) : y \in \mathrm{SE}\}, \\ E^{\mathrm{SE}}(f(x)) = \min\{f(x+y) : y \in \mathrm{SE}\}. \end{cases} \tag{1}$$

The dilation operator ($D(f(x))$) works as a maximal filter, which assigns the maximum value of pixel-values in the structure element to the one being investigated. It eliminates the dark details and widens the bright area in an image. Conversely, the erosion operator ($E(f(x))$) works as a minimal filter. It takes the minimum values of pixels in the structure element, and hence makes dark areas spread and light areas gather. Based on these two transformations, the opening ($O(f(x))$) of a grey level image $f(x)$ by SE is defined as follows

$$O^{\mathrm{SE}}(f(x)) = D^{\mathrm{SE}}(E^{\mathrm{SE}}(f(x)))\,. \tag{2}$$

The opening operator first applies the erosion transformation to the image, and then applies the dilation transformation. It suppresses the peak noise and then makes the image smoother. Furthermore,

the bright details with a smaller size than the structure element are eliminated but signals with similar geometric features in the structure element are preserved. Finally the top-hat transformation of a grey level image $f(x)$ by structure element (SE) is defined as

$$\mathrm{TH}^{\mathrm{SE}}(f(x)) = f(x) - O^{\mathrm{SE}}(f(x))\,. \tag{3}$$

The top-hat transformation first applies the opening operation to the image and then subtracts the resulting image from the original one. This process can be regarded as a non-linear high-pass filter. According to different geometric structure elements, the top-hat transformation can enhance or suppress information with various applications in the image. By the use of a proper structure element, the transformation discriminates star and debris images from the background in a simple way, and hence makes subtraction and segmentation easier. In addition, this transformation works in the spatial domain, so the computing process is fast enough for real-time data reduction.

2.2 Pipeline for Image Processing

The main package is implemented mostly in the language C++, based upon a set of C/Fortran libraries. Similar to the classic approach of SExtractor (Bertin & Arnouts 1996), the reduction process for optical space debris observation includes the following steps:

(1) Image loading;
(2) Bias/dark/flat calibration (if needed);
(3) Mathematical morphology filtering and enhancement;
(4) Global thresholding;
(5) Subtraction and segmentation;
(6) Determining the image positions in pixel coordinates.

According to the survey strategy, to optimize the detection sensitivity, the object tracking is applied during observations. Provided that prior information about a specific object is known, such as the projected CCD coordinates, the measured values of CCD coordinates can be easily obtained after a match up with the extracted sources in the neighborhood of the prior values. There are several specific features related to space debris observation, e.g. the relative movement between stars and objects and the large FOV of the telescope (generally greater than $2^\circ \times 2^\circ$). Most of the time, photometric results are not required, so a number of optimizations can be introduced to reduce the time cost and make the pipeline work more efficiently, as discussed below.

2.2.1 Input image

The CCD image is usually stored as a FITS file, and the image loading is performed with the CFITSIO libraries. Using these libraries, the raw image is loaded fast (generally less than 0.1 s for a 1k $\times$ 1k size image). In addition, the libraries are easy and convenient for system integration.

2.2.2 Image calibration

The calibration process includes the bias, dark and flat correction. It should be noticed that in space debris observation, the aim is mainly focused on achieving good quality in measurements of object coordinates, therefore, unless precise photometric results are needed, these corrections may be skipped, as they have negligible effects on the astrometric accuracy (Kouprianov 2008).

2.2.3 Image filtering

As described above, this step is the kernel of the whole pipeline. Due to the specific characteristic of the top-hat transformation, the selection of the structure element has a significant influence on the

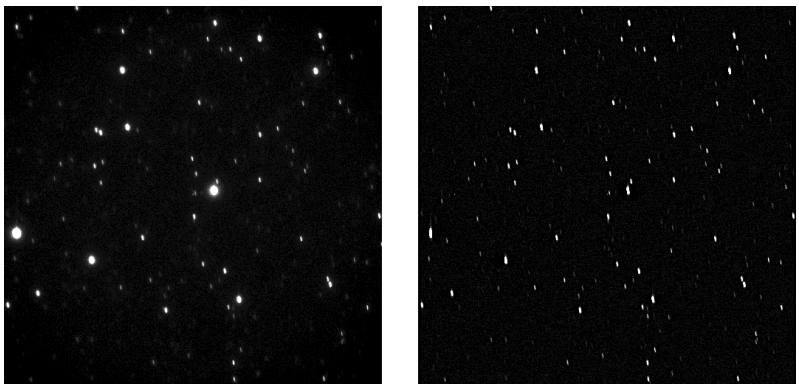

Fig. 1 The effect of the top-hat transformation. *Left*: The original image. *Right*: Image after it has been transformed with a structure element with size 7×1 pixels.

results. A large-sized structure element has a strong ability for noise elimination but loses the information at the image periphery and makes the image edge blurred; in addition, it is time consuming. On the other hand, a small-sized structure element keeps the information on the periphery, but has a weak ability for noise elimination and loses the continuity on the peripheries of the images.

For application, we take a rectangular structure element of size $x_1 \times x_2$. Considering that the top-hat transformation can only keep objects smaller than the structure element, we take the diameter of typical images to be the value of x_1; generally the values range from five pixels to 15 pixels, due to the fact that a longer exposure time makes star images wider by saturating the surrounding pixels. To reduce the time cost of the operation, the x_2 value is fixed to one pixel. The direction of the structure element can be chosen either along a line or column. A sample is shown in Figure 1; the distribution of pixel values is shown in Figure 2. It indicates that the global threshold can be applied after the transformation of the image. Although the values of the image are altered, as no photometric information is needed, this is negligible.

It is remarkable that the top-hat transformation can effectively eliminate the smear noise. The smear noise, which is induced by the absence of a shutter, forms during the charge transfer and erasure process. The noise is distributed along the same direction as the charge transfer, and hence it is either along a line or column. By the structure element defined above, the operation effectively removes the smear noise and improves the image quality. Furthermore, if we use the structure element which better fits the shape of the star trail, the blended images of objects and stars can be effectively separated, with a high degree of precision in the computed centroid. Because this paper is focused on developing a filtering process using mathematical morphology and source extraction, the details are beyond our discussion, and only the highlights are presented here.

2.2.4 Global thresholding

As shown above, due to the fact that the background may be highly non-uniform for wide-field sensors, induced by vignetting, light pollution, the Moon and clouds, etc., the application of a global threshold is infeasible. However, the top-hat transformation eliminates the background variations and makes the image smoother; at the same time the SNR of objects is improved, therefore it is well suited to apply the global threshold for image subtraction and segmentation, and hence the time cost of background estimation is reduced as well. The threshold can be given simply as

$$I_{\mathrm{t}} = B + k\delta\,, \tag{4}$$

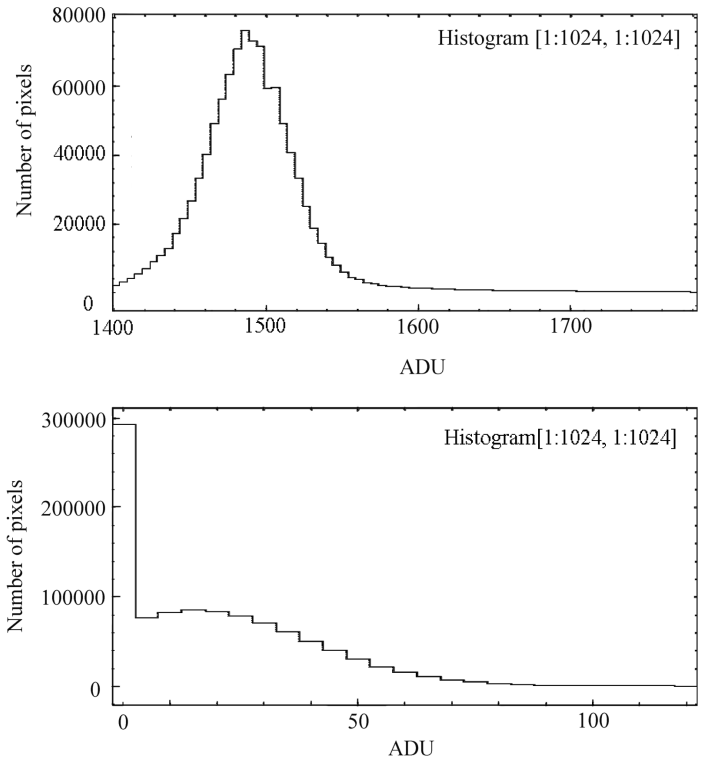

Fig. 2 The distribution of pixel values for images illustrated in Fig. 1. *Top*: Distribution of pixel values for the original image. *Bottom*: Distribution of pixel values for the image after being transformed with a structure element with size 7×1 pixels.

where B is the global background of the transformed image, which can be computed as the mean intensity across the whole image; δ is the root mean square of the image pixels, which can be taken as the noise level and k is the manually set threshold factor. Considering that a lack of reference stars makes the astrometric calibration infeasible and inaccurate, and that at the same time the detection ability for faint space debris must be assured, the threshold factor cannot be set too high. Generally, setting the values between $0.8 \sim 2$ is feasible, depending on the specific circumstances. After the background value is given, the thresholding is done automatically and produces a bit mask, which is an image consisting of only values 0 and 1.

$$M(x,y) = \begin{cases} 1 & I(x,y) \geq I_{\rm t}\,, \\ 0 & I(x,y) < I_{\rm t}. \end{cases} \tag{5}$$

2.2.5 Segmentation

The identification of individual objects above the detection threshold involves the connectivity properties of pixel groups, in which a kind of method based upon the detection of 8-connected groups of pixels is adopted. The implementation is based on a specific two pass union-finding algorithm (*http://www.astromatic.net/forum/showthread.php?tid=101*), which has been widely used in the past. It is noticeable that in this step, the minimum number of pixels $N_{\rm min}$ is introduced as

another threshold, a connected group of pixels with number less than $N_{\min}$ is not taken as a star or an object, and further information about these groups is discarded.

2.2.6 Barycenter positions

For the determination of image positions in pixel coordinates, the widely used point spread function (PSF) fitting technique seems to be the most robust and versatile way to obtain the image positions, with a high degree of precision (Stone 1989). The barycenter method gives a faster estimation of the astrometric position, but has poor accuracy. However, there are some specific issues that may arise in space debris observation, which are summarized as follows:

- The trails of stars and objects may overlap, which makes PSF fitting fail.
- Undersampling is a common problem for space debris observations, which decreases the accuracy of PSF fitting.
- For objects with low-SNRs or which are surrounded by a rapidly changing background (the latter situation is common for monitoring fast moving objects in low orbit), the estimation results from PSF fitting may be incorrect. It is demonstrated that for faint objects, barycenter positions are much more accurate.
- The PSF fitting method is more time consuming, compared to the barycenter technique.
- Rapid time variability of the object's brightness and image morphology, which is also common in objects with low orbits, contributes to the large errors in the PSF fitting results.

According to the above issues, in our pipeline we adopt the barycenter method, considering that it is the easiest and the most computationally effective technique, although it is more inaccurate than PSF fitting; the sub-pixel accuracy already meets the engineering requirement. The barycenter positions are calculated simply as

$$\begin{cases} X = \frac{\sum\limits_{i \in S} I_i x_i}{\sum\limits_{i \in S} I_i}, \\ Y = \frac{\sum\limits_{i \in S} I_i y_i}{\sum\limits_{i \in S} I_i}. \end{cases} \tag{6}$$

where S is the pixel group of the trail, (x_i, y_i) is the pixel coordinate, I_i is the (x_i, y_i) pixel value after subtracting the detection threshold, and (X, Y) is the barycenter position of the object.

3 APPLICATION

To analyze the feasibility and accuracy of our method, we make observations of the satellite "Ajisai," which acts as a reflector for laser targeting and orbits the Earth at an altitude of about 1500 km, and the GPS satellite with COSPAR ID 1996–019A, circling the Earth at an altitude of about 20 000 km. Both of the satellites are measured with extremely high accuracy in their orbits, and the extrapolated ephemeris of the two satellites exhibits a precision in position of better than 10 meters, satisfying the requirements of this work. In our experiments, we extrapolate the satellite ephemeris to the observing time, and then match the object in the neighboring area of the image, within the extracted sources, and finally, the corresponding equatorial coordinates of the objects are obtained by astrometric calibration. Through the comparison, we can obtain the residual errors, which demonstrates the accuracy of our technique.

During 20 nights, we have obtained more than 6000 frames for the two above objects, using two different optical sensors. The parameters of our images are shown in Table 1.

A couple of sample raw images are shown in Figure 3. The images are produced by our optical sensors that are specifically used for space debris observation. As in many wide field systems, the

Table 1 Parameters of Images

Sensor A		Sensor B	
Aperture of telescope	500 mm	Aperture of telescope	500 mm
Size of frame	1024×1024	Size of frame	2048×2048
FOV	$1.9^\circ \times 1.9^\circ$	FOV	$4.4^\circ \times 4.4^\circ$
Spatial sampling	$6.68''$	Spatial sampling	$7.73''$
CCD operating mode	Frame transfer	CCD operating mode	Full frame
Exposure time	50 ms $\sim$ 2000 ms	Exposure time	1000 ms $\sim$ 2000 ms
Number of observation arcs	21	Number of observation arcs	15

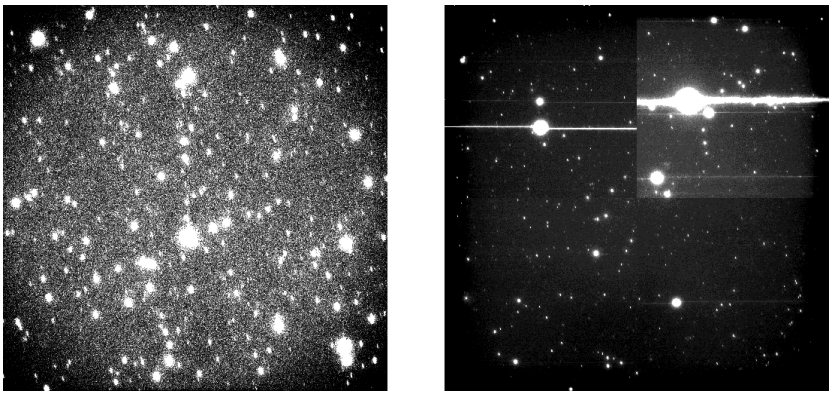

Fig. 3 *Left*: A raw image produced by sensor A. *Right*: A raw image produced by sensor B. Due to the absence of a shutter, the smear noise is obvious.

vignetting is obvious, and for the full frame CCD camera, the smear noise is ineluctable without the use of a shutter.

Due to the survey strategy and specific features of the optical sensor, for objects in low orbit, the detection threshold is set at 2, and $N_{\min}$ is set at 5.

$$I_{\mathrm{t}} = B + 2 \times \delta\,. \tag{7}$$

The size of the structure element is set at 7×1 pixels, along the linear direction. Experiments indicate that a smaller structure element size makes the signal of objects weaker and hence detection is difficult, although adopting a small size for the structure element makes the pipeline work faster; generally, a size of 9×1 increases the computing time by about 50% over a size of 5×1. Considering the rapid time variability in brightness and generally low SNR of the object (compared to objects in high orbit above Earth), it is feasible to apply these parameters. Eight consecutive frames with exposure times of 300 ms for Ajisai are shown in Figure 3, where the rapidly changing morphology of the object's image is obvious.

For objects in high orbit, due to the relatively long exposure time, the SNR is sufficiently high, the detection threshold is set at 1.2, $N_{\min}$ is also set at 5, and the size of the structure element is set at 7×1 pixels. The tests are made on a PC equipped with an Intel Core i7 cpu at 3.4 GHz and 4G of memory; no parallel computing is used and all the times given are calculated in this configuration.

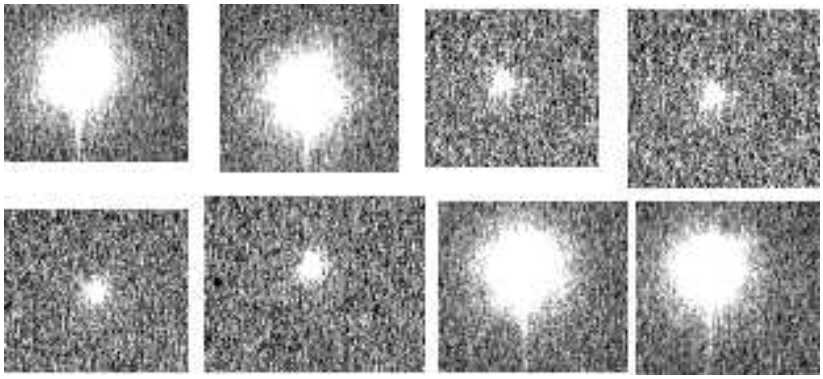

Fig. 4 The eight consecutive frames with exposure times of 300 ms for Ajisai.

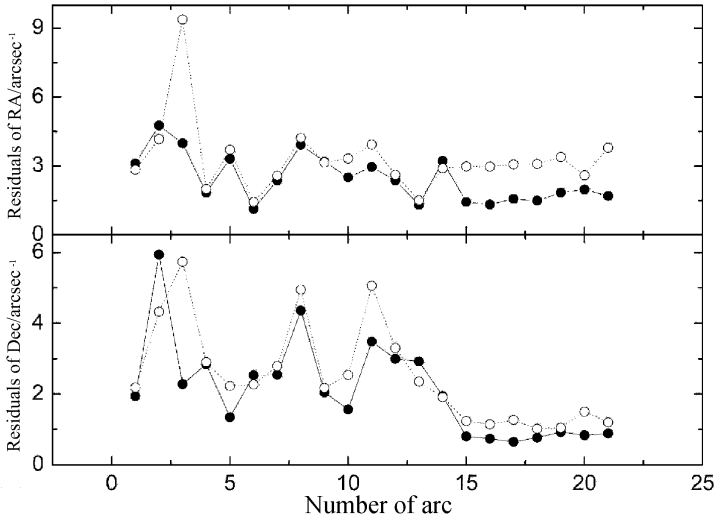

Fig. 5 The residuals, obtained by our method and SExtractor, of objects which are observed by sensor A. *Top*: The residuals of right ascension (*Filled circles*: Our method. *Open circles*: Source Extractor). *Bottom*: The residuals of declination.

4 RESULTS AND DISCUSSION

For comparison, we present the results obtained by our algorithm and the widely-used SExtractor software. For 1k $\times$ 1k images, the corresponding residuals are shown in Figure 5. It should be noticed that the observation arcs $1 \sim 14$ represent points from the Ajisai satellite, and the other arcs are from GPS satellites. It is demonstrated that for objects in low Earth orbit, our technique performs as accurately as SExtractor; in particular for most arcs, the residuals of right ascension range between $1''$ and $4''$, and the residuals of declination also range from $1''$ to $4''$. When the method is applied for objects in high Earth orbits, the accuracy is improved by about 100%. The residuals of right ascension are improved from $3''$ to $1.5''$, and the residuals of declination are improved from $1.2''$ to about $0.6''$.

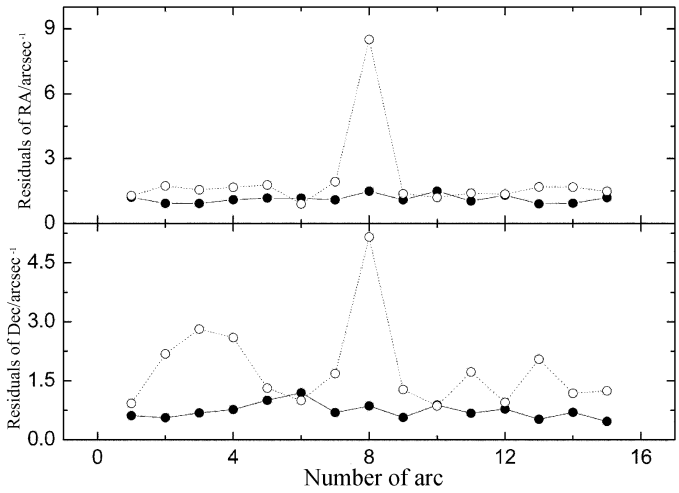

Fig. 6 The residuals obtained by our method and SExtractor of objects which are observed by sensor B. *Top*: The residuals of right ascension (*Filled circles*: Our method. *Open circles*: Source Extractor). *Bottom*: The residuals of declination.

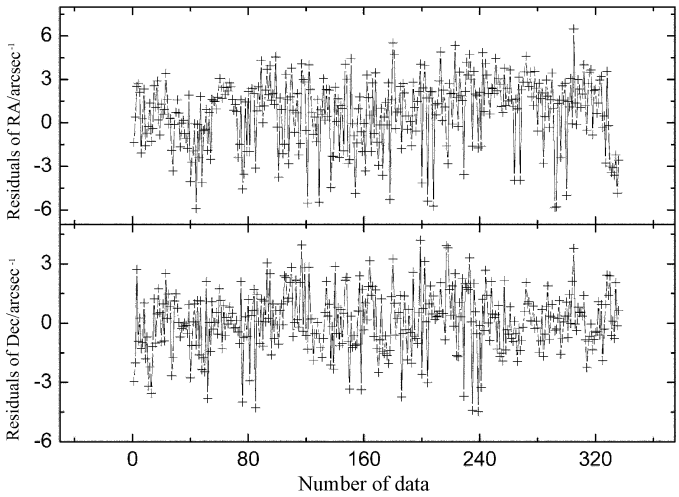

Fig. 7 The residuals of a whole arc of the Ajisai satellite observed by sensor A.

The corresponding results for application in 2k×2k images are shown in Figure 6; all of the arcs denote the GPS satellite in high-earth orbit. It indicates that the improvement in accuracy is the same as for the 1k×1k image; the accuracy in both right ascension and declination is increased by 100%, from about $1.5''$ to $0.8''$. The sources on the images are extracted with a high precision in computing the centroid. The residuals for the data taken from three observation arcs are shown in Figures 7, 8 and 9. In image processing, a larger size for the structure element leads to a slightly higher accuracy (no more than 10%), but also more computing time; at the same time, a higher detection threshold increases the accuracy but may deteriorate detections of an arc, hence, the choice of parameters is important.

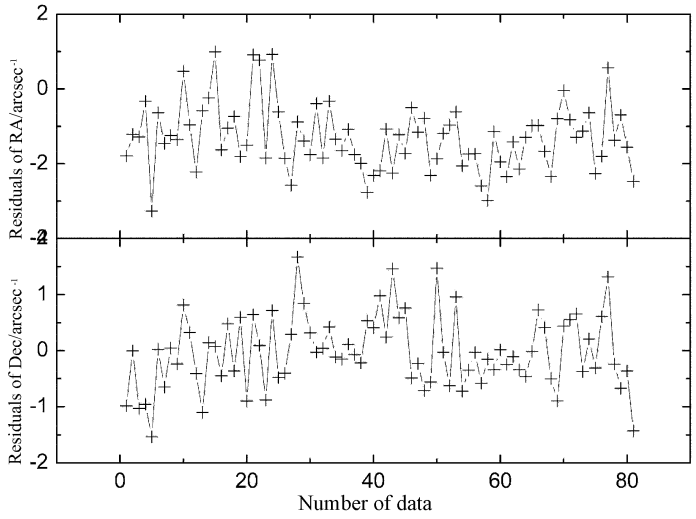

Fig. 8 The residuals of a whole arc of the GPS satellite observed by sensor A.

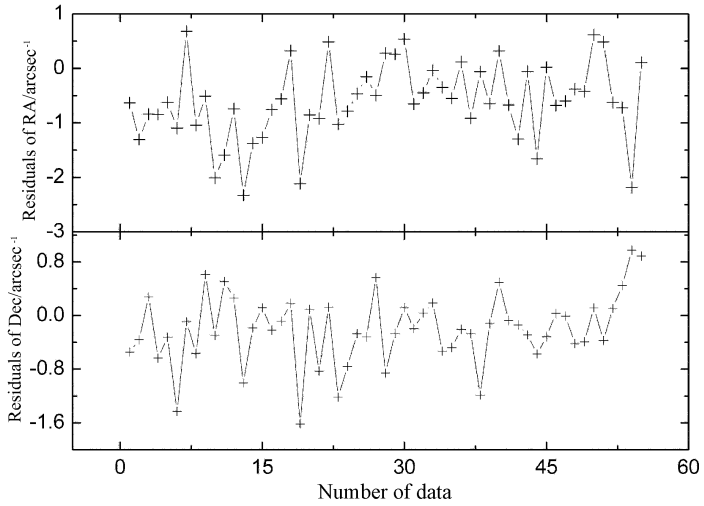

Fig. 9 The residuals of a whole arc of the GPS satellite observed by sensor B.

As we described above, an important requirement for image reduction is the ability to process the data in real-time. In our experiments, the full pipeline takes about 0.2 second for a 1k$\times$1k image and 0.8 second for a 2k$\times$2k image. If a smaller size of structure element is used, e.g. 5×1 pixels, the processing time can be reduced to less than 0.1 second. By contrast, the SExtractor takes about 0.4 second for a 1k$\times$1k image and more than 1.5 seconds for a 2k$\times$2k image. The improvement in computing efficiency is obvious. However, we should note that it is impossible to test the algorithm under all circumstances, hence the deficiencies and limitations should be recognized. As the algorithm is dedicated to data reduction of optical space debris observation, no photometric results are obtained and only position measurements are provided.

5 CONCLUSIONS

In this paper we described several challenges arising from the task of the real-time automatic reduction of optical space debris observations. An algorithm based on the mathematical morphology is presented and an entire pipeline is developed to solve these problems. These methods are implemented on a great quantity of images produced by our ground-based sensors that were specifically implemented for surveys of space debris. The results indicate that our innovative method is well suited for real-time data reduction of optical space debris observation. With respect to the widely-used SExtractor software, our method exhibits more accurate centroid positions and works faster; for objects in high-earth orbit the precision in position is improved by 100% and for objects in low-earth orbit the precision is maintained. Meanwhile, the computing time is halved, hence there is evident improvement. Therefore, currently it satisfies all the demands for data reduction of optical space debris observation, and can be widely used in the future.

Acknowledgements This work was funded by the National Natural Science Foundation of China (Grant Nos.11125315 and 11033009).

References

Alby, F., Boer, M., Deguine, B., et al. 2004, Advances in Space Research, 34, 1143
Bertin, E., & Arnouts, S. 1996, A&AS, 117, 393
Hebert, T. J., Africano, J. L., Stansbery, E. G., et al. 2001, Advances in Space Research, 28, 1283
Kouprianov, V. 2008, Advances in Space Research, 41, 1029
Laas-Bourez, M., Wailliez, S., Deleflie, F., et al. 2012, Advances in Space Research, 49, 603
Molotov, I., Agapov, V., Titenko, V., et al. 2008, Advances in Space Research, 41, 1022
Musci, R., Schildknecht, T., & Ploner, M. 2004, Advances in Space Research, 34, 912
Musci, R., Schildknecht, T., Ploner, M., & Beutler, G. 2005, Advances in Space Research, 35, 1236
Porfilio, M., Piergentili, F., & Graziani, F. 2004, Advances in Space Research, 34, 921
Rykhlova, L. V., Bagrov, A. V., Barabanov, S. I., et al. 2001, Advances in Space Research, 28, 1301
Schildknecht, T., Ploner, M., & Hugentobler, U. 2001, Advances in Space Research, 28, 1291
Schildknecht, T., Musci, R., Ploner, M., et al. 2004, Advances in Space Research, 34, 901
Schildknecht, T. 2007, A&A Rev., 14, 41
Schildknecht, T., Musci, R., & Flohrer, T. 2008, Advances in Space Research, 41, 1039
Seitzer, P., Smith, R., Africano, J., et al. 2004, Advances in Space Research, 34, 1139
Stone, R. C. 1989, AJ, 97, 1227
Sun R.-Y., & Zhao C.-Y. 2012, Progress In Astronomy, 30, 394
Sun, R. Y., Zhao, C. Y., Ping, Y. D., Xiong, J. N., & Zhang, C. 2012a, Acta Astronomica Sinica, 53, 80
Sun, R.-Y., Zhao, C.-Y., Ping, Y.-D., Xiong, J.-N., & Zhang, C. 2012b, Chinese Astronomy and Astrophysics, 36, 340
Sun, R., Zhao, C., & Zhang, Y. 2012c, Science in China G: Physics and Astronomy, 55, 1945